Preprint version 12th IFAC Symposium on Robot Control, Budapest, Hungary (2018)

A Truly Redundant Aerial Manipulator exploiting a Multi-directional Thrust Base

Markus Ryll * **Davide Bicego** ** **Antonio Franchi** **

* *CSAIL, Massachusetts Institute of Technology, Cambridge, USA (ryll@mit.edu)*
** *LAAS-CNRS, Université de Toulouse, CNRS, Toulouse, France ({davide.bicego, antonio.franchi}@laas.fr)*

Abstract: We present a novel aerial manipulator concept composed of a fully actuated hexarotor aerial vehicle and an n degree of freedom manipulator. Aiming at interaction tasks, we present a trajectory following control framework for the end-effector of the manipulator. The system is modeled in Euler-Lagrangian formalism and in Denavit-Hartenberg form. Benefiting from the redundancy of the system, we present several cost function strategies based on the projected gradient method to optimize the aerial manipulator behavior. The control framework is based on exact feedback linearization. In an advanced simulation section, we thoroughly present the robustness of the system and its limits in two typical configuration constituted by an 8 and a 10 degrees of freedom redundant aerial manipulator.

Keywords: Unmanned aerial robots, Redundant manipulators, Robot kinematics

1. INTRODUCTION

Nowadays, Unmanned Aerial Vehicles (UAVs) are extensively employed in different application scenarios like remote monitoring (Merino et al., 2012) and aerial photography, search and rescue missions like SHERPA (2013-2017) and to perform many other *contact-less* operations. In recent years, new research efforts have been made towards the accomplishment of aerial physical interaction tasks which require the UAV, equipped with one (or more) robotic manipulator(s), to get *in contact* with the surrounding environment. Some examples of such operations can be found in aerial manipulation and grasping (Mellinger et al., 2011), peg-in-hole (Ryll et al., 2017), structure assembly and decommissioning (Staub et al., 2018) and also cooperative transportation (Mellinger et al., 2010). Such a direction has also been fostered by European Projects like AeRoArms (2015-2019).

This new field of complex tasks yields new challenges in the mechanical structure, in the design of aerial manipulators (Orsag et al., 2013), in the modeling methodologies (Yang and Lee, 2014), and specially in the control. In the last years, we saw a development from UAVs equipped with simple gripper, towards highly complex n-degree of freedom (DoF) compliant manipulators (Yüksel et al., 2015), Baizid et al. (2015). As these complex manipulators can be in constant motion, the reaction forces can destabilize the flight and the interaction of the UAV. To circumvent this problem, an applicable control scheme is needed not only to ensure the stability of the platform, but also to allow a precise tracking of a desired trajectory of the manipulator end-effector.

To fulfill these requirements, several control schemes have been developed. An adaptive scheme has been presented in Antonelli and Cataldi (2014), which compensates the manipulator mass and forces due to its motion. Lippiello and Ruggiero (2012) follow a similar modeling approach with an underactuated quadrotor design for a Cartesian impedance control. An approach based on the Lagrangian formulation is presented in Yang and Lee (2014), while the controller is based on a backstepping-like end-effector tracking law. In Orsag et al. (2014) a dual arm manipulator is used in a valve turning scenario. A sequential Newton method for unconstrained optimal control is used in Garimella and Kobilarov (2015) for model-predictive control in pick and place tasks with an aerial manipulator and Kim et al. (2015) presents a work focused on the task of opening an unknown drawer.

In this paper we present a novel approach - the combination of a fully actuated hexarotor platform combined with an arbitrary n DoF manipulator. This new approach comes with the drawback of a more complex system compared to standard planar multirotor systems and higher internal forces but is beneficial in several points. Roll and pitch angles of the aerial platform can be controlled independently from the platform position (e.g., for more advanced obstacle avoidance), Franchi et al. (2018). A planar rotor system with in total the same number of DoFs, would need a manipulator with two additional DoFs. Standard aerial manipulating platforms are underactuated in the dynamics of their center of mass, e.g. Yang and Lee (2014). Thus, these systems are only able track trajectories that are smooth in C^4 for the lateral position. For the proposed system a smoothness C^2 is sufficient.

The contributions of our solution are, first of all, a novel combination of fully actuated aerial platform and redundant manipulator. At the best of our knowledge, this arrangement has never been thoroughly investigated so far. Secondly, we present an entire modeled, combining the aerial vehicle and the manipulator, making advantage of the well-known Denavit-Hartenberg parametrization. Thirdly, we propose a novel controller based on full feedback linearization of the dynamics and the exploitation of the system redundancy.

The structure of the paper is as follows. We will derive the dynamical model in Sec. 2. Afterwards, in Sec. 3 we will take advantage of the model to develop a controller based on feedback linearization and present a redundancy

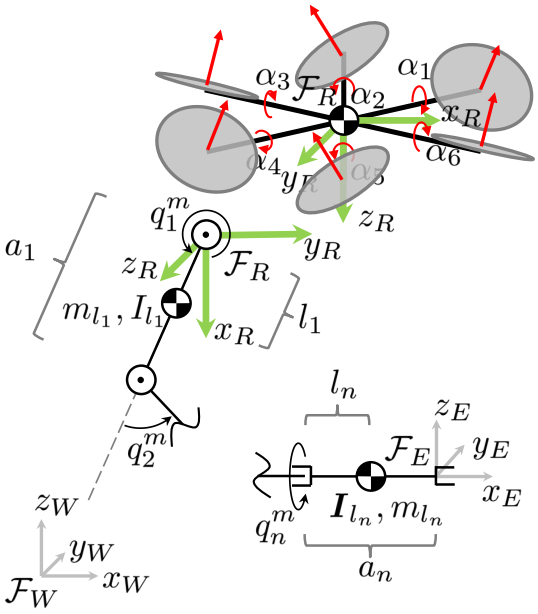

Fig. 1. Exemplary schematics of the considered aerial platform and the n-degree robotic arm. For clarity, the platform and the arm are drawn detached and the arm has been cut between link 2 and $n-1$. The following properties are presented: $\mathbf{I}_{l_i}$ - Moment of inertia of link i, m_{l_i} - mass of link i, a_i - distance between joint i and $i+1$, l_i - distance between joint i and CoG of link i, q_i - generalized coordinate of joint i.

exploitation approach, followed by Sec. 4 where we present a use-case scenario with a 2 and a 4 DoF manipulator. Based on this scenario, we test the validity of our control framework in practical case simulations in Sec. 5. Finally, we conclude the paper with an outline of our results and a hint of future works.

2. MODELING

In this work we consider an *aerial manipulator* composed by a *fully-actuated aerial vehicle* (in the following denoted as the 'aerial vehicle') and a *manipulator* mounted onboard of it. The aerial vehicle that we consider is a hexarotor with tilted propellers proposed in Rajappa et al. (2015). Fig. 1 provides a scheme of the aerial manipulator as well as the definition of the main symbols adopted in the paper, which are formally introduced in the following.

We start by defining a fixed *world frame*, $\mathcal{F}_W$, whose axes (unit vectors) are $\{\mathbf{x}_W, \mathbf{y}_W, \mathbf{z}_W\}$ and origin is O_W. Then we define two moving frames. The frame $\mathcal{F}_R : O_R - \{\mathbf{x}_R, \mathbf{y}_R, \mathbf{z}_R\}$ is rigidly attached to the aerial vehicle and its origin O_R coincides with the Center of Mass (CoM) of the aerial vehicle; whereas the frame $\mathcal{F}_E : O_E - \{\mathbf{x}_E, \mathbf{y}_E, \mathbf{z}_E\}$ is rigidly attached to the end-effector of the manipulator. The positions of O_R and O_E expressed in $\mathcal{F}_W$ are denoted with $\mathbf{p}_r \in \mathbb{R}^3$ and $\mathbf{p}_e \in \mathbb{R}^3$, respectively.

The aerial vehicle configuration in 3D space is fully described by $\mathbf{p}_r$ and by the rotation matrix $\mathbf{R}_r \in \mathsf{SO}(3)$ (where $\mathsf{SO}(3) = \{\mathbf{A} \in \mathbb{R}^{3\times3} | \mathbf{A}\mathbf{A}^T = \mathbf{I},\ det(A) = 1\}$), representing the rotation of $\mathcal{F}_R$ w.r.t. $\mathcal{F}_W$. The angular velocity of $\mathcal{F}_R$ with respect to $\mathcal{F}_W$, expressed in $\mathcal{F}_W$, is denoted with $\boldsymbol{\omega}_r \in \mathbb{R}^3$.

The manipulator has n degrees of freedom and we denote with $\mathbf{q}_m = [q_1^m \ \cdots \ q_n^m]^T \in \mathbb{R}^n$ its generalized coordinates, where q_i^m represents the i-th joint variable, with $i = 1 \dots n$. The end-effector configuration in 3D space is fully described by $\mathbf{p}_e$ and by the matrix $\mathbf{R}_e \in \mathsf{SO}(3)$, representing the rotation of $\mathcal{F}_E$ w.r.t. $\mathcal{F}_W$. The angular velocity of $\mathcal{F}_E$ with respect to $\mathcal{F}_W$, expressed in $\mathcal{F}_W$, is denoted with $\boldsymbol{\omega}_e \in \mathbb{R}^3$.

In order to use the Lagrangian approach we write the configuration of the aerial vehicle with a minimal set of generalized coordinates as $\mathbf{q}_r = [\mathbf{q}_{r1}^T \ \mathbf{q}_{r2}^T]^T \in \mathbb{R}^6$, where $\mathbf{q}_{r1} = \mathbf{p}_r$, and $\mathbf{q}_{r2} = \boldsymbol{\eta} = [\phi \ \theta \ \psi]^T$ is a minimal parameterization of $\mathbf{R}_r$, like, e.g., the roll, pitch, and yaw angles. Finally, we denote with $\mathbf{T}_{\boldsymbol{\eta}}$ the matrix such that $\boldsymbol{\omega}_r = \mathbf{T}_{\boldsymbol{\eta}}\dot{\boldsymbol{\eta}}$. We will show in Sec. 3.2 that using minimal representation is not restrictive in our case as the attitude of the aerial vehicle will not exceed near hovering condition. The complete configuration of the aerial manipulator is then described by $\mathbf{q} = [\mathbf{q}_r^T \ \mathbf{q}_m^T]^T \in \mathbb{R}^{6+n}$.

The dynamical model of the aerial manipulator is easily derived applying the Euler-Lagrange equation to the kinetic and potential energy of the system, thus obtaining

$$\mathbf{M}(\mathbf{q})\ddot{\mathbf{q}} + \mathbf{c}(\mathbf{q}, \dot{\mathbf{q}}) + \mathbf{d}(\dot{\mathbf{q}}) + \mathbf{g}(\mathbf{q}) = \begin{bmatrix} \boldsymbol{\tau}_r \\ \boldsymbol{\tau}_e \end{bmatrix}, \tag{1}$$

where $\mathbf{M}(\mathbf{q}) \in \mathbb{R}^{(6+n)\times(6+n)}$ is the positive definite inertia matrix of the whole aerial manipulator, $\mathbf{c}(\mathbf{q}, \dot{\mathbf{q}}) \in \mathbb{R}^{6+n}$ contains all the centrifugal and Coriolis terms, $\mathbf{d}(\dot{\mathbf{q}}) \in \mathbb{R}^{6+n}$ contains the friction terms, $\mathbf{g}(\mathbf{q})$ contains all the gravity terms, and $\boldsymbol{\tau}_r \in \mathbb{R}^6$ and $\boldsymbol{\tau}_e \in \mathbb{R}^n$ are the control wrench applied to the aerial vehicle and the control torques applied to each joint of the manipulator, respectively. This approach is thoroughly presented in Lippiello and Ruggiero (2012).

The wrench $\boldsymbol{\tau}_r$ can be decomposed in a 3D force and a 3D moment (Rajappa et al., 2015), i.e.,

$$\boldsymbol{\tau}_r = \begin{bmatrix} \boldsymbol{\tau}_{r1} \\ \boldsymbol{\tau}_{r2} \end{bmatrix} = \begin{bmatrix} \boldsymbol{\tau}_{r1} \\ \boldsymbol{\tau}_{\text{thrust}} + \boldsymbol{\tau}_{\text{drag}} \end{bmatrix}, \tag{2}$$

where the single components are computed as

$$\boldsymbol{\tau}_{r1} = k_f \mathbf{R}_r \sum_{i=1}^{6} \mathbf{R}_{p_i,\alpha}^r \mathbf{e}_3 w_i, \tag{3}$$

where k_f is the propeller force coefficient, $\mathbf{R}_{p_i,\alpha}^r$ is the constant rotation matrix expressing the orientation of the i-th propeller with respect to $\mathcal{F}_R$, $\mathbf{e}_3 = [0\ 0\ 1]^T$, and w_i is the square of the spinning velocity of the i-th propeller;

$$\boldsymbol{\tau}_{\text{thrust}} = k_f \mathbf{R}_r \sum_{i=1}^{6} \left(\mathbf{p}_i^R \times \mathbf{R}_{p_i,\alpha}^r \mathbf{e}_3 w_i \right), \tag{4}$$

where $\mathbf{p}_i^R \in \mathbb{R}^3$ is the constant position of the center of the i-th propeller expressed in $\mathcal{F}_R$; and

$$\boldsymbol{\tau}_{\text{drag}} = k_d \mathbf{R}_r \sum_{i=1}^{6} \mathbf{R}_{p_i,\alpha}^r \mathbf{e}_3 (-1)^i w_i, \tag{5}$$

where k_d is the propeller drag coefficient. The factor $(-1)^i$ in (5) is used to take into account the contrariwise spinning velocity of every second propeller. The subscript in $\mathbf{R}_{p_i,\alpha}^r$ denotes the dependency on the angle $\alpha \in (0, \pi/2]$, which represents the amount of tilting of the i-th propeller about the direction of $\mathbf{p}_i^R$.

Replacing (3), (4), and (5) in (2) one can compactly write

$$\boldsymbol{\tau}_r = \mathbf{G}_{\mathbf{w}}(\boldsymbol{\eta}, \alpha)\mathbf{w}, \tag{6}$$

where $\mathbf{w} = [\hat{w}_1\ \hat{w}_2\ \hat{w}_3\ \hat{w}_4\ \hat{w}_5\ \hat{w}_6]^T$, where $\hat{w}_i = \text{sign}(w_i)w_i^2$ and $\mathbf{G}_\mathbf{w}(\boldsymbol{\eta}, \alpha) \in \mathbb{R}^{6\times6}$. Equation (6) can be used to replace $\boldsymbol{\tau}_r$ in (1) in order to explicitly show the dependence of the dynamics on $\mathbf{w}$.

The matrix $\mathbf{G}_\mathbf{w}(\boldsymbol{\eta}, \alpha)$ plays a crucial role in the actuation capabilities of the aerial vehicle. If α is 0 then all the propellers would be coplanar and the aerial vehicle would be underactuated, with $\mathbf{G}_\mathbf{w}$ being non invertible and degrading the system to an ordinary coplanar hexarotor. If $0 < \alpha < \frac{\pi}{2}$ then $\mathbf{G}_\mathbf{w}$ results invertible for any $\boldsymbol{\eta}$ and the aerial vehicle is fully actuated. However if the aerial vehicle is too much tilted (i.e., when ϕ and θ are too large) the inversion $\mathbf{w} = \mathbf{G}_\mathbf{w}^{-1}(\boldsymbol{\eta}, \alpha)\boldsymbol{\tau}_r$ might return non-positive values in one or more entries of $\mathbf{w}$ thus resulting in an unfeasible command. It is then important to keep ϕ and θ within the operating condition that guarantee the full-actuation with positive propeller spinning velocities (see Sec. 3.2).

3. CONTROL

The control problem considered in this work is to let $\mathbf{p}_e$ and $\mathbf{R}_e$ exactly track a desired arbitrary trajectory expressed as $(\mathbf{p}_e^d(t), \mathbf{R}_e^d(t)) \in \mathbb{R}^3 \times SO(3)$, while exploiting the redundancy to possibly optimize additional requirements. We assume that $(\mathbf{p}_e^d(t), \mathbf{R}_e^d(t)) \in \bar{C}^3$ and that $(\dot{\mathbf{p}}_e^d(t), \boldsymbol{\omega}_e^d(t))$, and $(\dot{\mathbf{p}}_e^d(t), \dot{\boldsymbol{\omega}}_e^d(t))$ are also provided, as customary.

In order to achieve such an objective let us start from replacing $\boldsymbol{\tau}_r$ from (6) in (1), thus obtaining

$$\mathbf{M}(\mathbf{q})\ddot{\mathbf{q}} + \mathbf{c}(\mathbf{q}, \dot{\mathbf{q}}) + \mathbf{d}(\dot{\mathbf{q}}) + \mathbf{g}(\mathbf{q}) = \mathbf{K}(\boldsymbol{\eta}, \alpha) \begin{bmatrix} \mathbf{w} \\ \boldsymbol{\tau}_e \end{bmatrix}, \quad (7)$$

where

$$\mathbf{K}(\boldsymbol{\eta}, \alpha) = \begin{bmatrix} \mathbf{G}_\mathbf{w}(\boldsymbol{\eta}, \alpha) & \mathbf{0} \\ \mathbf{0} & \mathbf{I}_n \end{bmatrix} \in \mathbb{R}^{6+n\times6+n}.$$

We then first apply the following inner control loop

$$\begin{bmatrix} \mathbf{w} \\ \boldsymbol{\tau}_e \end{bmatrix} = \mathbf{K}^{-1}\Big(\mathbf{M}\mathbf{u}_q + \mathbf{c} + \mathbf{d} + \mathbf{g}\Big), \quad (8)$$

where we omitted the dependency from $\mathbf{q}$ and $\dot{\mathbf{q}}$ for brevity. Control (8) brings the dynamics of $\mathbf{q}$ in the fully linearized and decoupled form

$$\ddot{\mathbf{q}} = \mathbf{u}_q,$$

where $\mathbf{u}_q$ is an additional virtual input. Notice that this result is not possible for standard aerial manipulators using coplanar multi-rotors as aerial platform.

As customary, see, e.g., Siciliano et al. (2009) the differential kinematics of the aerial manipulator can be expressed as

$$\mathbf{v}_e = \begin{bmatrix} \dot{\mathbf{p}}_e \\ \boldsymbol{\omega}_e \end{bmatrix} = \begin{bmatrix} \dot{\mathbf{p}}_r \\ \boldsymbol{\omega}_r \end{bmatrix} + \mathbf{J}_m(\mathbf{q}_m)\dot{\mathbf{q}}_m = \mathbf{J}(\mathbf{q})\dot{\mathbf{q}}, \quad (9)$$

where $\mathbf{J}_m(\mathbf{q})$ and $\mathbf{J}(\mathbf{q})$ are the geometric Jacobians of the manipulator and of the complete aerial manipulator, respectively. By differentiating (9) we obtain the dynamics of the end-effector configuration

$$\dot{\mathbf{v}}_e = \dot{\mathbf{J}}(\mathbf{q}, \dot{\mathbf{q}})\dot{\mathbf{q}} + \mathbf{J}(\mathbf{q})\ddot{\mathbf{q}} = \dot{\mathbf{J}}(\mathbf{q}, \dot{\mathbf{q}})\dot{\mathbf{q}} + \mathbf{J}(\mathbf{q})\mathbf{u}_q \quad (10)$$

where we applied the inner control loop (8).

Using the fact that $\mathbf{J}$ has always full rank for any $\theta \neq \pi(k+\frac{1}{2})$ with $k \in \mathbb{Z}$ (see Sec. 3.1) as typically done, we choose the virtual input $\mathbf{u}_q$ as

$$\mathbf{u}_q = \mathbf{J}(\mathbf{q})^\dagger(\mathbf{u}_e - \dot{\mathbf{J}}(\dot{\mathbf{q}}, \mathbf{q})\dot{\mathbf{q}}) + \big(\mathbf{I}_{6+n} - \mathbf{J}(\mathbf{q})^\dagger\mathbf{J}(\mathbf{q})\big)\mathbf{z} \quad (11)$$

with $[]^\dagger$ being the Moore-Penrose inverse of the argument and $\mathbf{u}_e$ and $\mathbf{z}$ two additional virtual inputs. Under the effect of the second inner control loop (11) the dynamics of the end-effector task becomes exactly linearized and fully decoupled

$$\dot{\mathbf{v}}_e = \mathbf{u}_e = \begin{bmatrix} \mathbf{u}_{e_1} \\ \mathbf{u}_{e_2} \end{bmatrix},$$

regardless of the choice of the second input $\mathbf{z}$, whose use will be defined later. Now we are able to solve the desired control problem stated at the beginning of this section, i.e., the exact asymptotic tracking of a desired trajectory For the end-effector position it is sufficient to use

$$\mathbf{u}_{e_1} = \ddot{\mathbf{p}}_d + \mathbf{K}_{P_1}(\dot{\mathbf{p}}_e^d - \dot{\mathbf{p}}_e) + \mathbf{K}_{P_2}(\mathbf{p}_e^d - \mathbf{p}_e) \quad (12)$$

in (11) to obtain exponential and decoupled position error convergence where $\mathbf{K}_{P_1}, \mathbf{K}_{P_2}$ define a Hurwitz polynomial. For the orientation of the end-effector it is instead sufficient to choose

$$\mathbf{u}_{e_2} = \dot{\boldsymbol{\omega}}_e^d + \mathbf{K}_{\omega_1}(\boldsymbol{\omega}_e^d - \boldsymbol{\omega}_e) + \mathbf{K}_{\omega_2}\mathbf{e}_R \quad (13)$$

with the orientation error defined as

$$\mathbf{e}_R = \frac{1}{2}[\mathbf{R}_e^T\mathbf{R}_e^d - \mathbf{R}_e^{dT}\mathbf{R}_e]_\vee \quad (14)$$

where $[]_\vee$ represents the inverse map from $so(3)$ to $\mathbb{R}^3$ (Lee et al., 2010) and $\mathbf{K}_{\omega_1}, \mathbf{K}_{\omega_2}$ define a Hurwitz polynomial as well.

The task Jacobian matrix $\mathbf{J}$ possesses an n-dimensional null space onto which the additional control input $\mathbf{z}$ is projected, see (11). The use of $\mathbf{z} \in \mathbb{R}^{6+n}$ to fulfill additional tasks besides the tracking of a desired trajectory is discussed in Section 3.2.

3.1 Full-rankness of $\mathbf{J}$

In order to demonstrate that $\mathbf{J}$ is always full rank, it is sufficient to prove that it exists a $[6 \times 6]$ submatrix of $\boldsymbol{J}$ which is invertible. For convenience let us choose the following submatrix of $\mathbf{J}$

$$\mathbf{A} = \begin{bmatrix} j_{11} & \cdots & j_{16} \\ \vdots & \ddots & \vdots \\ j_{61} & \cdots & j_{66} \end{bmatrix} \quad (15)$$

the determinant of $\mathbf{A}$ can be found to be

$$\det(\mathbf{A}) = \cos(\theta). \quad (16)$$

It follows that $\mathsf{rank}(\mathbf{J}) = 6$ for any $\theta \neq \pi(k+\frac{1}{2})$ with $k \in \mathbb{Z}$. In fact this corresponds to the singularity of the roll, pitch, yaw representation. Notice that this holds independently from the kind of manipulator mounted onboard of the aerial vehicle.

3.2 Redundancy Exploitation

In this section we discuss the exploitation of the n-dimensional redundancy of the system by designing a control law for the additional input $\mathbf{z}$ in (11) using the projected gradient method (De Luca et al., 1992). As optimization criteria to be fulfilled by the redundancy exploitation we opt for

(1) *Horizontal aerial vehicle orientation:* Notice that if $\dot{\mathbf{q}} = \mathbf{0}$, the most efficient configuration in terms of propeller spinning velocities is with $\theta = 0$ and $\phi = 0$. Therefore the optimization based on H_1 shall automatically drive the system to a state close to $\theta = \phi = 0$. By carefully selecting maximum angles for θ and ϕ we can achieve a bounded behavior of the control output $\boldsymbol{w}$ in (8).

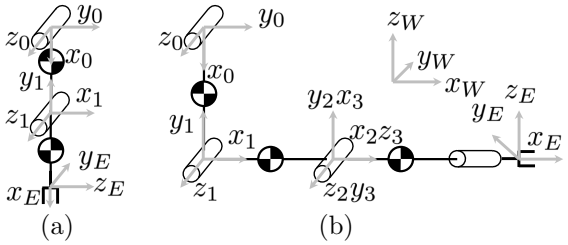

Fig. 2. Schematic side view of the two considered manipulators. (a) The two joints rotate about the same axis in an elbow manner. (b) The manipulator (a) is extended by a third elbow joint and a last wrist like joint.

(2) *Obstacle avoidance*: The aerial manipulator is meant to interact with the environment using its end-effector. Consequently any other collision must be avoided. Especially any collision with the propellers would usually result in a highly critical situation. We therefore seek to maximize the distance between the aerial vehicle and surrounding obstacles. The aerial vehicle is encapsulate in a virtual cylinder, mimicking the shape of the aerial vehicle. A shortest vector between an arbitrary obstacle $\boldsymbol{O}_O$ and a point $\boldsymbol{o}_C$ on the cylinder $\boldsymbol{O}_C$ causes a virtual force acting on the point $\boldsymbol{o}_C$. The magnitude is inverse to the actual vector length. The virtual force results in a force and torque with respect to the aerial robot's CoM that drives the aerial vehicle to avoid the obstacle. To augment this virtual force the cost function H_2 is utilized.

(3) *Limitation of arm joints*: To prevent manipulator self-collisions and collisions between the manipulator and the aerial platform a cost function H_3 is utilized.

Minimization of the three objectives concordant with the output tracking task can be achieved by choosing

$$\mathbf{z} = \nabla_q H_1 + \nabla_q H_2 + \nabla_q H_3 \tag{17}$$

where $\nabla_{[]}$ is the gradient with respect to the variables [].

We are now in the state to compose the individual cost functions. We choose H_1 as

$$H_1(\boldsymbol{q}) = \frac{1}{2n} k_1 \sum_{i=4}^{5} \tan^2(\gamma q_i) \tag{18}$$

with $\gamma = \frac{\pi}{2k_{\phi,\theta}}$ and k_1 as suitable scalar gain and $k_{\phi,\theta}$ as maximum tilting angle. H_2 is selected as

$$H_2(\boldsymbol{q}) = k_2 f(\min_{\mathbf{o_o}\in\mathbf{O}_o, \mathbf{o_R}\in\mathbf{O}_R} \|\mathbf{o}_c(\mathbf{q}) - \mathbf{o_R}\|) \tag{19}$$

with $\mathbf{o}$ being an obstacle point and O the set of obstacle points. $f()$ is a function mapping the obstacle distance to a force and a torque acting on the aerial robot's CoM and k_2 a suitable scalar gain.

And finally the third cost function is similarly defined as

$$H_3(\boldsymbol{q}) = \frac{1}{2n} k_3 \sum_{i=7}^{n-1} \tan^2(\gamma q_i) \tag{20}$$

with $\gamma = \frac{\pi}{2k_{\text{arm}}}$ and k_3 as suitable scalar gain and k_{arm} as maximum arm angle.

4. USE-CASE SCENARIO

In order to concretely present the general system described so far, let us now focus on two use case scenarios, first (1) a system with a 2 DoF manipulator depicted in Fig. 2-(a) and second (2) a system with a 4 DoF manipulator depicted in Fig. 2-(b). In both scenarios, all the links of the manipulator lay in the $\{\mathbf{x}_R, \mathbf{y}_R\}$ plane of $\mathcal{F}_R$. The first example realizes two elbow joints, while the second example extends the first by a third elbow-joint and a final wrist. The Denavit-Hartenberg parameters of the manipulators can be found in Tab. 1. These configurations have been purposefully chosen driven by the idea that the aerial vehicle can primarily be in charge of the desired end-effector position and its yaw orientation, while the remaining orientation quantities can be primarily controlled by the manipulator. The total number of degrees of freedom of the aerial manipulator, with $n + 6 = 8$ and $n + 6 = 10$, still leaves extra maneuvering room for the exploitation of the redundancy.

4.1 Added Uncertainties and Simplifications

We decided to test the robustness of the controller against a model with realistic uncertainties. Based on previous experiences, we firstly added to all model parameters a Gaussian distributed uncertainty with different standard deviations depending on the measurability of the property (mass properties: $\sigma_1 = 0.01$, length properties: $\sigma_2 = 0.02$, inertia properties: $\sigma_3 = 0.05$). The controller is fed with the nominal property values while the model contains the altered real values. Secondly, we considered communication delays, control quantization effects and actuation noise on the propellers and joint actuation. Thirdly we overlaid sensor measurements (e.g. joint position, aerial robot position and their derivatives) with a realistic noise profile. Fourthly the dynamics of the brushless controllers and the propellers are modeled with a first order transfer function whereas the controller is based on the presented model. Finally, for simplicity we neglected the effects due to motors and gear boxes driving the manipulator joints.

5. NUMERICAL VALIDATION

In this section we present the simulation results to validate the presented control framework. Firstly, we present results of two trajectory tracking experiments (I & II) with configuration (1) demonstrating the general tracking capabilities of the system and the benefits of the optimization. Secondly, we will show the robustness of the method with a Monte Carlo experiment (III) exploiting configuration (2). The interested reader is referred to a video (`https://youtu.be/9DBKfToHWGM`) showing the presented experiments in detail.

5.1 General Tracking and Optimization Benefits

In experiment (I) the end-effector of the manipulator shall track a desired trajectory describing a 360 deg rotation about the end-effector axis y_e (see Fig.2-(a) and Fig. 4-(a)) while keeping the position constant. A time-lapse picture of the trajectory is depicted in Fig. 3. The end-effector tracking error remains marginal during the maneuver with a maximum position error $max(|e_e|) < 0.02\ m$ (see Fig. 4-(b & c)). Thanks to the optimization in Sec. 3.2 the

Table 1. Denavit-Hartenberg parameters of the considered manipulator (compare with Fig. 2).

Link	a_1	α_i	d_i	υ_i
1	a_1	0	0	υ_1
2	a_2	0	0	υ_2
3	0	$\frac{\pi}{2}$	0	$\frac{\pi}{2} + \upsilon_3$
4	0	0	$a_3 + a_4$	υ_4

Fig. 3. Time-lapse picture of the aerial manipulator during experiment (I). The end-effector performs a full rotation while the position is constant. Thanks to the optimization the aerial vehicle remains almost horizontal. For clarity: the single time instances are presented next to each other, while in reality, the small red dot in all pictures overlaps.

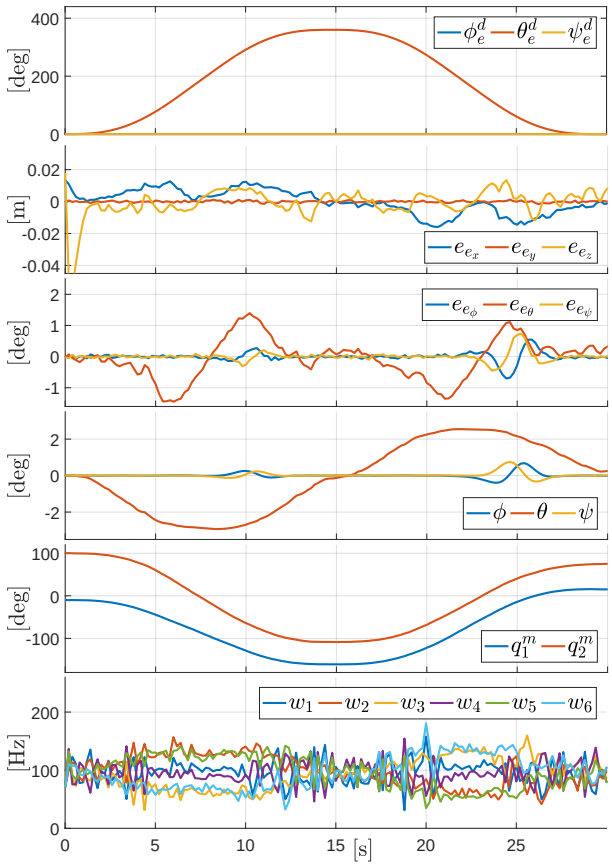

Fig. 4. Full rotation in spot of the end-effector: (a) Desired orientation expressed in Euler angles; (b) end-effector position tracking error; (c) end-effector orientation tracking error; (d) Actual orientation of the aerial vehicle expressed in Euler angles; (e) angle of the n-th joints; (f) propeller spinning velocities.

tilting angle of the aerial vehicle remains small and the rotor spinning velocity bounded (4-(d & e))

In experiment (II) the end-effector of the manipulator shall track a translational trajectory $\boldsymbol{p}_e^d$ parallel to the world frame axis $\mathbf{x}_W$. The desired orientation $\boldsymbol{R}_e^d$ of the end-effector remains constant. Given the initial state of the robot the aerial vehicle would collide with an obstacle that lies in the way of the trajectory (see Fig. 5). To track the trajectory safely, the aerial robot has to exploit its redundancy and change the position of the aerial robot with respect to the end-effector. It is obvious that the aerial vehicle performs a complex trajectory in order to avoid the obstacle. Thanks to the redundancy exploitation in (19) this capability is achieved.

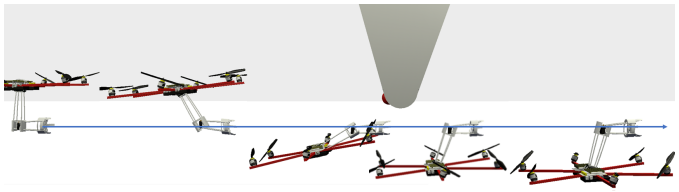

Fig. 5. Time-laps picture of the aerial robot avoiding an obstacle. The end-effector is tracking the translational trajectory (blue line) while the aerial vehicle automatically dodges the obstacle.

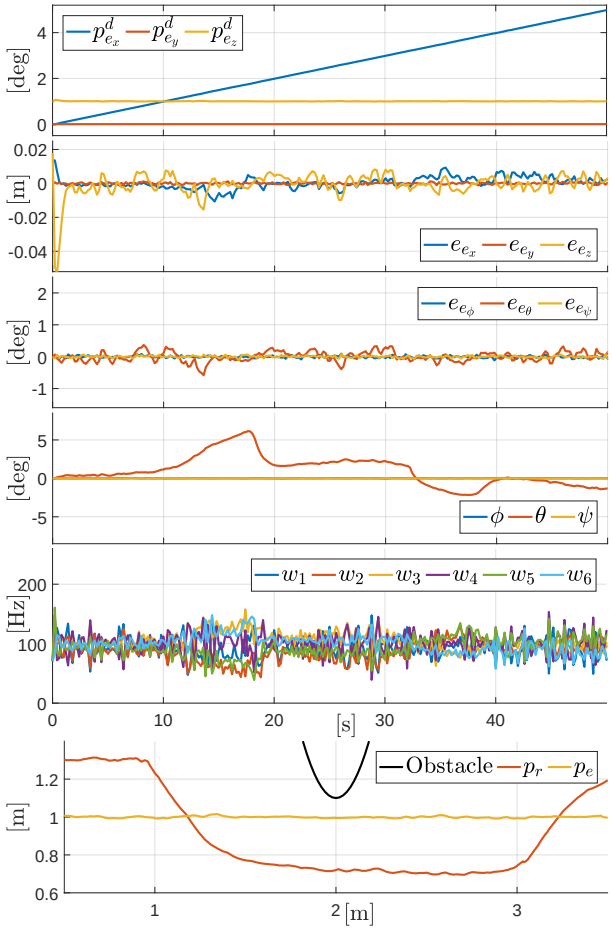

Fig. 6. Translational trajectory of the end-effector: (a) Desired position for the end-effector; (b) end-effector position tracking error; (c) end-effector orientation tracking error; (d) Actual orientation of the aerial vehicle expressed in Euler angles; (e) propeller spinning velocities; (f) position of the end-effector and the aerial vehicle in the x-z plane representation.

Fig. 6 presents the results of experiment (II). The first plot of Fig. 6 presents the desired trajectory of experiment (II). While following the desired trajectory the translational error and orientation error remain very small (plot two and three). The orientation of the aerial vehicle remains as well almost horizontal, with a maximum pitch angle of $\theta = 6$ deg. The fifth plot shows the actual spinning velocity of the six propeller. It is clear that all propeller rates stay positive and close to the nominal horizontal spinning velocity. Finally, the last plot depicts the position of the aerial vehicle and the end-effector in the x-z plane.

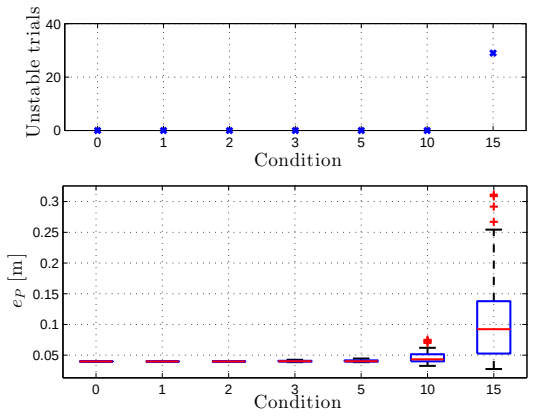

Fig. 7. Upper figure: Number of trials where instability was reached out 100 trials. With increasing uncertainties the number of unstable trials increases. Lower figure: Box plot of the Monte Carlo simulation showing the position error $\boldsymbol{e}_p$ in the different conditions k.

5.2 Monte Carlo Simulation

To further test the stability of our system and to find its limits we conducted a Monte Carlo simulation on configuration (2). In the simulation we follow an eight-shaped trajectory while increasing the uncertainties of the model (see Sec. 4.1) by multiplying the expected uncertainty with a constant parameter k. In every condition of the Monte Carlo simulation, we performed the individual simulations 100 times with randomized modeling error distribution. In total we executed seven conditions with an increasing standard deviation of a truncated Gaussian distribution (truncated at two standard deviations) as follows $k[\sigma_1\ \sigma_2\ \sigma_3]$ with k=[0 1 2 3 5 10 15]. In Fig. 7 the results are presented. It becomes clear that with an increasing uncertainty the performance degrades. Additionally, with a very high uncertainty, trials become unstable. This is expected as the controller cannot deal with extreme modeling errors. Anyway, even with a ten times higher uncertainty than expected no trials are unstable.

6. CONCLUSION

In this paper we presented a novel aerial manipulator based on a fully actuated aerial vehicle and an n-degree of freedom manipulator. We derived the dynamical model as well as the Denavit-Hartenberg parameters for the system. Then, we developed a controller based on feedback linearization aiming at trajectory tracking with the end-effector. Using an optimization scheme, we exploited the redundancy by optimizing the rotor spinning velocities (by keeping the platform horizontal), the aerial vehicle position and the manipulator joints positions. In an intense simulation and evaluation section we presented the capabilities of the aerial manipulator and as well showed the robustness of the system and its limits in a Monte Carlo simulation.

7. ACKNOWLEDGEMENTS

This work has been funded by the European Union's Horizon 2020 research and innovation programme under grant agreement No 644271 AEROARMS.

REFERENCES

AeRoArms (2015-2019). EU Coll. Proj. ICT-644271. `www.aeroarms-project.eu`.

Antonelli, G. and Cataldi, E. (2014). Adaptive control of arm-equippedquadrotors - theory and simulations. In *22th Mediterranean Conf. on Control and Automation*, 14461451.

Baizid, K., Giglio, G., Pierri, F., Trujillo, M.A., Antonelli, G., Caccavale, F., Viguria, A., Chiaverini, S., and Ollero, A. (2015). Experiments on behavioral coordinated control of an unmanned aerial vehicle manipulator system. In *IEEE International Conference on Robotics and Automation, ICRA 2015, Seattle, WA, USA, 26-30 May, 2015*, 4680–4685. doi:10.1109/ICRA.2015.7139848. URL `http://dx.doi.org/10.1109/ICRA.2015.7139848`.

De Luca, A., Oriolo, G., and Siciliano, B. (1992). Robot redundancy resolution at the acceleration level. *Laboratory Robotics and Automation*, 4, 97–97.

Franchi, A., Carli, R., Bicego, D., and Ryll, M. (2018). Full-pose tracking control for aerial robotic systems with laterally-bounded input force. *IEEE Trans. on Robotics*, 34(2), 534–541. doi:10.1109/TRO.2017.2786734.

Garimella, G. and Kobilarov, M. (2015). Towards model-predictive control for aerial pick-and-place. In *Robotics and Automation (ICRA), 2015 IEEE International Conference on*, 4692–4697. doi:10.1109/ICRA.2015.7139850.

Kim, S., Seo, H., and Kim, H. (2015). Operating an unknown drawer using an aerial manipulator. In *Robotics and Automation (ICRA), 2015 IEEE International Conference on*, 5503–5508. doi:10.1109/ICRA.2015.7139968.

Lee, T., Leoky, M., and McClamroch, N. (2010). Geometric tracking control of a quadrotor uav on se(3). In *Decision and Control (CDC), 2010 49th IEEE Conference on*, 5420–5425. doi:10.1109/CDC.2010.5717652.

Lippiello, V. and Ruggiero, F. (2012). Cartesian impedance control of a uav with a robotic arm. In *10th International IFAC Symposium on Robot Control*, 704–709.

Mellinger, D., Lindsey, Q., Shomin, M., and Kumar, V. (2011). Design, modeling, estimation and control for aerial grasping and manipulation. In *2011 IEEE/RSJ Int. Conf. on Intelligent Robots and Systems*, 2668–2673. San Francisco, CA.

Mellinger, D., Shomin, M., Michael, N., and Kumar, V. (2010). Cooperative grasping and transport using multiple quadrotors. In *10th Int. Symp. on Distributed Autonomous Robotic Systems*, 545–558. Lausanne, Switzerland.

Merino, L., Caballero, F., Martnez-de Dios, J., Maza, I., and Ollero, A. (2012). An unmanned aircraft system for automatic forest fire monitoring and measurement. *Journal of Intelligent and Robotic Systems*, 65(1-4), 533–548. doi:10.1007/s10846-011-9560-x. URL `http://dx.doi.org/10.1007/s10846-011-9560-x`.

Orsag, M., Korpela, C., Bogdan, S., and Oh, P. (2014). Valve turning using a dual-arm aerial manipulator. In *Unmanned Aircraft Systems (ICUAS), 2014 International Conference on*, 836–841. doi:10.1109/ICUAS.2014.6842330.

Orsag, M., Korpela, C., and Oh, P. (2013). Modeling and control of MM-UAV: Mobile manipulating unmanned aerial vehicle. *Journal of Intelligent & Robotics Systems*, 69(1-4), 227–240.

Rajappa, S., Ryll, M., Bülthoff, H.H., and Franchi, A. (2015). Modeling, control and design optimization for a fully-actuated hexarotor aerial vehicle with tilted propellers. In *2015 IEEE Int. Conf. on Robotics and Automation*, 4006–4013. Seattle, WA.

Ryll, M., Muscio, G., Pierri, F., Cataldi, E., Antonelli, G., Caccavale, F., and Franchi, A. (2017). 6D physical interaction with a fully actuated aerial robot. In *2017 IEEE Int. Conf. on Robotics and Automation*, 5190–5195. Singapore.

SHERPA (2013-2017). EU Integ. Proj. IP 600958. `www.sherpa-project.eu`.

Siciliano, B., Sciavicco, L., Villani, L., and Oriolo, G. (2009). *Robotics: Modelling, Planning and Control*. Springer.

Staub, N., Bicego, D., Sablé, Q., Arellano-Quintana, V., Mishra, S., and Franchi, A. (2018). Towards a flying assistant paradigm: the OTHex. In *2018 IEEE Int. Conf. on Robotics and Automation*. Brisbane, Australia.

Yang, H. and Lee, D. (2014). Dynamics and control of quadrotor with robotic manipulator. In *Robotics and Automation (ICRA), 2014 IEEE International Conference on*, 5544–5549. doi:10.1109/ICRA.2014.6907674.

Yüksel, B., Mahboubi, S., Secchi, C., Bülthoff, H.H., and Franchi, A. (2015). Design, identification and experimental testing of a light-weight flexible-joint arm for aerial physical interaction. In *2015 IEEE Int. Conf. on Robotics and Automation*, 870–876. Seattle, WA.